

Low dimensional nanostructures of fast ion conducting lithium nitride

Nuria Tapia-Ruiz^{1,#,+}, Alexandra G. Gordon^{2,#}, Catherine M. Jewell¹, Hannah K. Edwards^{2,3}, Charles W. Dunnill¹, James M. Blackman⁴, Colin P. Snape⁴, Paul D. Brown³, Ian MacLaren⁵, Matteo Baldoni^{2,6}, Elena Besley², Jeremy J. Titman² and Duncan H. Gregory^{1,*}

¹WestCHEM, School of Chemistry, University of Glasgow, Glasgow G12 8QQ, UK.

²School of Chemistry, University of Nottingham, University Park, Nottingham NG7 2RD, UK

³Department of Mechanical, Materials and Manufacturing Engineering, University of Nottingham, University Park, Nottingham NG7 2RD, UK.

⁴Department of Chemical and Environmental Engineering, University of Nottingham, University Park, Nottingham NG7 2RD, UK.

⁵School of Physics and Astronomy, University of Glasgow, Glasgow G12 8QQ, UK.

⁶Istituto per lo Studio dei Materiali Nanostrutturati (ISMN), Consiglio Nazionale delle Ricerche (CNR), Via P. Gobetti 101, 40129 Bologna, Italy

#These authors contributed equally to this work;

*Corresponding author: Duncan.Gregory@glasgow.ac.uk +Current address: Department of Chemistry, Lancaster University, Lancaster LA1 4YB

Abstract

As the only stable binary compound formed between an alkali metal and nitrogen, lithium nitride possesses remarkable properties and is a model material for energy applications involving the transport of lithium ions. Following a materials design principle drawn from broad structural analogies to hexagonal graphene and boron nitride, we demonstrate that such low dimensional structures can also be formed from an s-block element and nitrogen. Both one- and two-dimensional nanostructures of lithium nitride, Li₃N, can be grown despite the absence of an equivalent van der Waals gap. Lithium-ion diffusion is enhanced compared to the bulk compound, yielding materials with exceptional ionic mobility. Li₃N demonstrates the conceptual assembly of ionic inorganic nanostructures from monolayers without the requirement of a van der Waals gap. Computational studies reveal an electronic structure mediated by the number of Li-N layers, with a transition from a bulk narrow-bandgap semiconductor to a metal at the nanoscale.

Introduction

Lithium nitride, Li₃N, was originally proposed for use as an electrolyte in all-solid-state Li⁺ ion batteries given its exceptional ionic conductivity at room temperature (ca. 10⁻³ S cm⁻¹)¹. Indeed, for several decades it remained the highest conducting crystalline Li⁺ ion conductor at ambient conditions hampered chiefly by its low decomposition potential despite many ongoing attempts to stabilise it. Doping with late transition metals, however, triggers electronic conductivity that can be exploited in anodes with more than twice the charging capacity of graphite². Li₃N has also been proposed for a myriad of other applications, e.g. as a means of converting CO₂ into useful products³, as the electron injection layer (EIL) in organic light-emitting diodes (OLEDs)⁴ and as an unusual reducing agent in preparative organic and organometallic chemistry⁵. Further, in 2002 Li₃N was

43 revealed as a potential candidate for solid-state hydrogen storage given its capability to
44 accommodate up to 10.4 wt.% H₂⁶. Slow kinetics for H₂ sorption and high (de)hydrogenation
45 temperatures are the primary hurdles to overcome before the Li-N-H system can be exploited
46 commercially, however. By combining experiment and calculation, we demonstrate how the changes
47 in electronic structure and reduction of diffusion lengths brought about by chemically
48 nanostructuring Li₃N can lead to dramatic changes in electronic properties and ionic transport
49 behaviour.

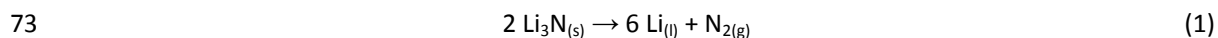
50

51 **Results**

52 **Synthesis and characterisation**

53 Li₃N nanocrystals grow following the heating and cooling of the bulk nitride powder under a reduced
54 pressure of nitrogen (see Methods). Powder X-ray diffraction (PXD) data for the fine powder product
55 matches to hexagonal α -Li₃N (*P6/mmm*; *a* = 3.656(2) Å; *c* = 3.868(4) Å) (Supplementary Figure 1). In
56 the nanofibre syntheses, long structures with diameters ranging from 200 nm to 2 μ m and lengths in
57 excess of 10 μ m were produced (Fig. 1). Atomic force microscopy (AFM) measurements confirmed
58 these ranges of thicknesses in the different fibres observed (Supplementary Figure 2). The
59 morphology of the nanostructured material can be tailored by controlling the preparative conditions
60 to yield different types of nanofibres (see Methods).

61 The growth of the 1D nanostructures can be rationalised in terms of a self-assisted vapour-
62 liquid-solid (VLS) mechanism. Under vacuum, Li₃N will decompose at a temperature below the
63 ambient pressure decomposition temperature (815 °C; $\Delta H_{(298K)} = -171.3 \pm 7.7 \text{ kJ mol}^{-1}$)^{7,8} (Eq. 1),
64 forming droplets of liquid Li, since the melting point of Li (*T* = 180.5 °C) lies well below the applied
65 reaction temperatures. These Li seeds would act as nucleation sites for the N_{2(g)} species, which
66 supersaturate the Li droplets and eventually lead to anisotropic growth and Li₃N fibre formation.
67 Energy-dispersive X-ray spectroscopy (EDX) data of the fibrous material did not show any traces of
68 other metals such as Fe (from the wire used to support the reaction vessel), ruling out the possibility
69 of Fe acting as a catalyst or seed for the formation of the fibres described here (Supplementary
70 Figure 3). Self-catalytic growth of GaN nanowires from Ga droplets and gallium/nitrogen vapour
71 species has been observed previously⁹. The comparison to GaN is apposite in that both binary
72 nitrides are formed from low melting point metals.



74

75 Two types of single-crystalline straight fibres with different growth orientations (I and II) form under
76 varying reaction conditions (see Supplementary Tables 1 and 2): type I nanofibres (Figs. 2a-b) exhibit
77 a growth direction of $\langle 10\bar{1}0 \rangle$ whereas, conversely, type II nanofibres exhibit a growth direction of
78 $\langle 0001 \rangle$ (Figs. 2c-d). Typically, type II nanofibres were found together with a few fibres and
79 nanosheets with zig-zag morphology (Supplementary Figures 4 and 5). Thus, Li₃N nanofibres exist in
80 which the hexagonal [Li₂N] layers are stacked either parallel or perpendicular to the principal fibre
81 axis. Carbon nanofibres can assemble in an analogous fashion, where graphene layers can be
82 oriented either perpendicular or parallel to the principal fibre axis^{10,11}. Our experimental evidence
83 shows that the pressure within the reaction vessel is likely to be the crucial parameter for the
84 preferential growth of type I and II nanofibres; i.e. under identical reaction times and temperature,
85 type II fibres will be favoured over type I fibres at higher reaction pressures (Supplementary Tables 1
86 and 2). There are several examples in the literature that describe how the total pressure and/or

precursor partial pressure can control the growth direction of fibres; these preferences can be both thermodynamically and kinetically driven¹². Indeed, in this respect, our density functional theory (DFT) calculations suggest that type I nanofibres (-325.44 eV Li₃N unit⁻¹) are more thermodynamically stable than the equivalent type II fibres (-324.59 eV Li₃N unit⁻¹). The dependence of growth direction on seed concentration in layered BN and GaN fibres has been previously reported¹³. Moreover, it has been well-documented that nanowire growth direction is directly impacted by pressure across diverse systems of varying complexity (e.g. in semiconductors such as Si, In₂O₃ and InN)¹⁴⁻¹⁷. One might expect an increased Li seed concentration at elevated reaction pressure. An increase in N₂ partial pressure (concentration) and the N:Li ratio at the growth interface should lead to the formation of Li-N planes and type II fibre propagation. Local variation in pressure and N:Li stoichiometry might, therefore, account for the formation of zig-zag (kinked) nanofibres and sheets observed in type II samples (Supplementary Figures 4 and 5); analogous behaviour has been noted for Si and InN nanowires, for example.^{15,16}

Raman spectra from nanostructured Li₃N (fibres type I and type II) and bulk Li₃N showed one prominent peak at ca. 580 cm⁻¹, attributable to the only Raman active mode of Li₃N, i.e. E_{2g} (Supplementary Figure 6). This phonon mode corresponds to the displacement of the Li(2) and N atoms along the *ab* plane in Li₃N¹⁸ and is consistent with group theory predictions and the spectra of bulk Li₃N¹⁹. We found that the E_{2g} mode band was slightly blue-shifted (by ca. 5 cm⁻¹) with respect to the bulk for both type I and type II fibres. Raman spectra of microcrystals of structurally-similar graphite and BN^{20,21} and of BN nanotubes²² also revealed that the E_{2g} band broadens and shifts to a higher frequency as particle size decreases. Ab-initio calculations on BN single-walled nanotubes (SWNTs) attribute the blue shift in the E_{2g} mode (of 5 cm⁻¹) to a shortening of the sp² bonds with respect to the bulk²². The additional bands observed at ca. 500 cm⁻¹ and 700 cm⁻¹ in both bulk and nanoscale Li₃N samples were assigned to the acoustic (A) and optical phonon (O) modes 2 TA (z, K), 2 TO(A) and 2 LA(A) (T= transverse, L = longitudinal) by direct comparison with the second-order Raman spectra of Li₃N²³. A band corresponding to the second-order phonon mode was also observed at 350 cm⁻¹ (2 LA (M, K)). The presence of these modes is attributed to the resonant conditions established when using laser irradiation, i.e. at 2.33 eV²⁴.

The layered crystal structure of Li₃N (hexagonal *P6/mmm*) shares salient symmetry features with those of hexagonal graphite and BN. [Li₂N] layers contain Li atoms in trigonal planar coordination to N, ostensibly by analogy to sp² hybridised carbon in the graphene layers of graphite or to boron and nitrogen in BN (Fig. 3)¹. Given the formation of anisotropic fibres (types I and II; Fig. 3) like layered chalcogenides, MX₂ (M = early transition metal; X = S, Se), it may be tempting to classify Li₃N as an extension of this latter class of materials²⁵. Importantly, however, what distinguishes Li₃N from the above examples is the absence of a van der Waals gap; although anisotropic, Li₃N is connected in the third dimension by Li atoms (forming infinite [-Li-N-Li-] chains).

Li⁺ and H⁺ transport properties

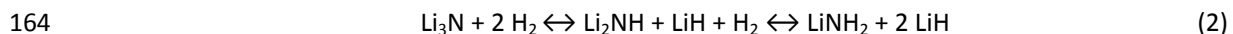
Given the exceptional Li⁺ fast ionic conducting properties of bulk Li₃N, we wished to understand how the ionic transport might vary as a consequence of nanostructuring. Variable-temperature (VT) wide-line ⁷Li solid-state nuclear magnetic resonance (NMR) measurements between 133 and 373 K enabled the local structure of the type I and type II nanofibres to be probed and allowed the Li⁺ ion transport properties of the Li₃N nanofibres to be determined (Fig. 4, Supplementary Note 2 and Supplementary Figures 7 and 8). The line narrowing observed particularly for the Li(2) satellite lines between 133 K and 293 K can be interpreted in terms of intra-layer Li⁺ diffusion, by analogy with the

132 corresponding behaviour for bulk Li_3N^{26} . Similarly, the broadening that occurs above 293 K and
133 eventually causes both sets of satellites to disappear into the baseline results from inter-layer
134 diffusion via an exchange of Li^+ between the Li(1) and Li(2) sites. Assuming simple Arrhenius
135 behaviour, the activation energy for the former intra-layer process can be measured from the
136 temperature variation of the linewidth and was found to be 0.075 and 0.053 eV for type I and II Li_3N
137 nanofibres respectively, which should be compared with the value of 0.121 eV, previously obtained
138 for bulk Li_3N^{27} (Supplementary Table 3). Hence, Li^+ ion hopping becomes more facile within the Li-N
139 planes as a result of nanofibre formation. Electrochemical impedance spectroscopy measurements
140 were attempted on these samples to corroborate the conductivity results obtained by NMR.
141 However, the high temperatures required to sinter pellets pressed from the Li_3N nanofibres (i.e. to
142 reduce grain boundary resistances) compromised their nanostructured morphology, so although
143 high values of conductivity could be obtained (ca. $1 \times 10^{-3} \text{ S cm}^{-1}$), we could not treat the data
144 obtained as representative of the fibres.

145 High Li^+ ion conductivity is a fundamental requirement for solid electrolytes to compete against
146 organic electrolytes in lithium-ion batteries. To date, only a few sulphide-type electrolytes have
147 shown comparable ionic conductivities to commercial organic electrolytes²⁸. Thus, nanostructuring
148 of solid electrolytes might be a plausible approach to increase ionic conductivity. This field is only at
149 its infancy, with most of the work conducted on the $\text{Li}_7\text{La}_3\text{Zr}_2\text{O}_{12}$ (LLZO) garnet solid electrolyte (as a
150 sintered ceramic or as an inorganic filler component in solid composite polymer electrolytes)²⁹.
151 Nevertheless, given the low decomposition potential of Li_3N (ca. 0.45 V vs. Li^+/Li)³⁰ and the enhanced
152 electronic conductivity expected in these nanostructured materials when compared to the bulk (see
153 DFT calculations section), the use of Li_3N as a solid electrolyte seems implausible from a practical
154 point of view. On the other hand, in lithium-containing hydrogen storage materials, e.g. the lithium
155 amide-lithium imide system, proton mobility has been intrinsically-linked to Li^+ ion diffusion³¹.
156 Hence, we expected that the high Li^+ ion mobility observed in these Li_3N nanofibres may lead to
157 improved hydrogen absorption properties.

158 Preliminary volumetric experiments to determine the hydrogen uptake properties of the
159 nanostructured Li_3N material were conducted by differential pressure analysis (DPA). As compared
160 to bulk samples of highly crystalline, single-phase Li_3N , the initial H_2 uptake for the nano- Li_3N
161 material was found to be lower (8.9 wt% vs. 10.5 wt%). The latter uptake is typical for pristine bulk
162 material and matches the theoretical capacity from a two-step reaction mechanism (Eq. 2)⁶:

163



165

166 One might postulate that the reduction in initial gravimetric capacity in the nanofibres is a result
167 of surface hydrolysis (passivation) on handling in air (as observed from transmission electron
168 microscopy (TEM)/selected area electron diffraction (SAED) experiments; Supplementary Note 1 and
169 Supplementary Figure 9). Nevertheless, there is a greater than three-fold increase in the rate of
170 hydrogen sorption for nanocrystalline Li_3N with respect to the bulk material in the first cycle, which
171 dramatically improves further in subsequent uptake cycles (Supplementary Figure 10). The
172 microstructure of the dehydrogenated nitride is retained through cycling (from imide to amide and
173 vice versa) and hence the (de)hydrogenation process is pseudomorphic and reversible
174 (Supplementary Figure 11). The enhanced hydrogen uptake behaviour of the nanofibres is broadly
175 analogous to the uptake kinetics observed when Li_3N is impregnated in mesoporous carbon or used
176 in carbon nanocomposites (also at a reduced sorption temperature of 200 °C and which exhibit a

177 hydrogen desorption enthalpy that is half that of the bulk material)³². Unlike these composites,
178 however, the nanofibres do not suffer from the gravimetric capacity penalty imposed by an inactive
179 component. Computational studies have demonstrated that pseudo-molecular $(\text{Li}_3\text{N})_n$ ($n= 1-7$)
180 clusters would bind H_2 via coordinatively-unsaturated Li atoms with an adsorption energy
181 approximately an order of magnitude smaller than that of the bulk material³³. By extension, earlier
182 DFT calculations show that the most favourable adsorption sites for both H_2 and dissociated H atoms
183 are to N positions on the (001) surface of Li_3N ³⁴. Semi-quantitatively at least, both prior studies
184 would indicate that fabrication of narrow nanofibres or thin nanosheets of Li_3N should produce
185 storage materials with improved sorption kinetics. Thus, the design and optimisation of anisotropic
186 Li-N(-H) nanomaterials could prove a useful strategy towards attaining a storage solution that meets
187 the challenging criteria required for implementing hydrogen as a fuel for transport. Further studies
188 should establish whether this is indeed the case.

189

190 **Calculations on nanostructured α - Li_3N electronic properties**

191 Electronic properties were computed on α - Li_3N using density functional theory (DFT), to compare
192 the behaviour of a monolayer of Li_3N with respect to the bulk material and to develop an
193 understanding of the evolution of electronic structure with the number of layers as compared to
194 graphene and other van der Waals nanostructures (vdWNs). Our calculations confirm that bulk α -
195 Li_3N is a semiconductor with an indirect bandgap of $E_g = 1.3$ eV, in agreement with several previous
196 first-principles calculations of the α - Li_3N electronic properties³⁵⁻³⁸. The electronic bandgap predicted
197 by DFT is notably smaller than the experimental optical band gap of 2.18 eV for Li_3N single crystals³⁹.
198 This discrepancy is due to the well-known DFT problem in underestimating conduction band state
199 energies⁴⁰⁻⁴¹. Unlike layers in vdWNs, a single $[\text{Li}_2\text{N}]$ layer is unstable and computational optimisation
200 produces two monolayer structures from the combination of $[\text{Li}_2\text{N}]$ and $[\text{Li}]$ planes, forms 1 and 2
201 (Figs. 5a-b), of which the latter is more stable by -0.574 eV.

202 Although the profile of the single-layer density of states (DOS) more closely resembles that of the
203 bulk material for the form 2 monolayer, both single layer forms are predicted to be metallic (Fig. 5c).
204 In each case, the DOS below and approaching the Fermi level is attributable to N states whereas the
205 higher states of the conduction band are composed predominantly of Li states. As the number of
206 layers in a Li_3N slab is increased, the total DOS at the Fermi level decreases and a clear tendency
207 towards an opening of a bandgap is observed (Fig. 5d). Li_3N nanosheets composed of up to 20 layers
208 (75.6 Å thick), for example, remain metallic, although using accurate quantum chemical approaches
209 it is difficult to predict a critical thickness at which the metal-semiconductor transition occurs. The
210 evolution of the electronic structure contrasts markedly with graphene, where there is a relatively
211 abrupt change from zero bandgap semiconducting to semi-metallic graphite-like behaviour as the
212 number of stacked monolayers increases⁴². Experimental data suggest that the bandgap in BN 5-
213 layer nanosheets (5.56 eV) is smaller than that calculated for a BN monolayer (6 eV), but both values
214 are larger than that of the bulk material (5.2-5.4 eV) and the nitride remains an insulator⁴³⁻⁴⁵.

215

216 **Discussion**

217 In summary, anisotropic 1D Li_3N nanostructured materials can be formed by broad analogy to sp^2 -
218 like layered solids such as graphite and boron nitride, despite the absence of a van der Waals gap in
219 Li_3N . Two distinct types of Li_3N fibres have been identified, here denoted as Type I and Type II, which
220 differ in the orientation of the $[\text{Li}_2\text{N}]$ layers (parallel or perpendicular) with respect to the long axis of
221 the fibre. The formation of 1D structural variants of Li_3N has important consequences for the

222 transport of Li^+ (and H^+) ions, which lead to demonstrable differences in diffusion behaviour
223 compared to the bulk material. DFT calculations have shown that the electronic properties of these
224 Li_3N materials appear scalable with size and shape.

225 Given their predicted metallic-like behaviour and high Li^+ ion mobility, we anticipate that these
226 nano-based Li_3N materials could play an important role as additives in high-power Li-based batteries,
227 which demand rapid ionic and electronic kinetics. Currently, bulk and surface-passivated Li_3N has
228 been used as a pre-lithiation additive in various cathode materials (e.g. LCO, NMC)^{46,47} to offset the
229 first-cycle lithium loss and thus, to improve the overall energy density of the material. Furthermore,
230 bulk Li_3N has been used as a protective coating for Li metal anodes in Li-ion and Li-S batteries to
231 avoid dendrite growth and parasitic reactions between polysulfides and Li metal^{48,49}. Importantly,
232 the nanostructured materials allow for the rapid growth of an insulating surface passivation layer
233 (e.g. formed from Li_2CO_3) conferring higher chemical stability which could eliminate reactions at the
234 electrolyte interface. From a different perspective, the superior Li^+ ion diffusion in the Li_3N
235 nanofibers leads to improved hydrogen absorption/desorption properties in the Li-N-H system given
236 the intrinsic relationship between proton and lithium-ion conduction in this system. Thus, by
237 analogy, it may be conceivable to revisit other materials related to the Li-N-H family of compounds
238 to explore the impact of nanoscaling on hydrogen storage and generation more widely.

239 Our studies clearly demonstrate that combining an s-block element with nitrogen under the
240 appropriate synthetic conditions can lead to the formation of anisotropic nanomaterials.
241 Nanostructuring has a palpable influence on many chemical and physical properties in the Li-N
242 system and there are likely to be other exciting phenomena and behaviours to be discovered. We
243 expect that this work will stimulate further research on this system and those containing other s-
244 block elements.

245

246 **Methods**

247 **Synthesis of type I Li_3N nanofibres.** $\alpha\text{-Li}_3\text{N}$ (ca. 0.1 g) prepared from the nitridation of a
248 sodium/lithium alloy²⁷ was contained within an iron foil liner that was placed inside a stainless-steel
249 crucible. The crucible was suspended by an iron wire inside a long, 3 cm internal diameter stainless
250 steel reaction vessel that was water-cooled at the upper end. The vessel was evacuated to a
251 pressure of ca. 5 Pa (a range of 4-6.7 Pa), then sealed and heated to 1023-1073 K in a vertical
252 furnace for 6 days. Finally, the furnace was cooled to room temperature. Supplementary Table 1
253 provides detailed reaction conditions for each of the syntheses performed that yielded Type I Li_3N
254 nanofibres.

255

256 **Synthesis of type II Li_3N nanofibres.** $\alpha\text{-Li}_3\text{N}$ (ca. 0.1 g) prepared from the nitridation of a
257 sodium/lithium alloy²⁷ was contained within an iron foil liner that was placed inside a stainless-steel
258 crucible. The crucible was suspended by an iron wire inside a long, 1.5 cm internal diameter stainless
259 steel reaction vessel that was water-cooled at the upper end. The vessel was evacuated to a
260 pressure of ca. 10 Pa (a range of 9.3-10.7 Pa), then sealed and heated to 1023-1073 K in a vertical
261 furnace for 6 days. Finally, the furnace was cooled to room temperature. Supplementary Table 2
262 shows detailed reaction conditions for each of the syntheses performed that yielded Type II Li_3N
263 nanofibres.

264 The handling of the reactants and products took place in a nitrogen-filled glovebox (Saffron Scientific
265 Ltd.; $\text{O}_2 < 5$ ppm; $\text{H}_2\text{O} < 10$ ppm) during the syntheses of both types of nanofibres. In both cases, on

266 cooling, red/dark purple fibrous material (10-40 mg) was found deposited on the Fe wire above the
267 reaction crucible. EDX spectra of all nanomaterials reveal peaks only from nitrogen (and oxygen from
268 brief air exposure). Given that Li is not detectable by EDX and that no peaks from lithium metal (or
269 other Li-containing phases) are observed in solid-state NMR spectra, the results are consistent with
270 the presence of single-phase Li_3N . The absence of metal impurity peaks corroborates a self-assisted
271 growth mechanism.

272

273

274 **Powder X-ray diffraction (PXD).** PXD data were collected using a Philips X'Pert θ - 2θ diffractometer
275 with a PW3710 control unit using Cu $K\alpha$ radiation ($\lambda = 1.5418 \text{ \AA}$), operating at 40 kV and 40 mA.
276 Samples were run within a bespoke air-tight aluminium holder with Mylar windows⁵⁰. Data were
277 collected in the range from 5 - 80 ° 2θ in steps of 0.025 ° s^{-1} . Sample preparation for analysis took
278 place in an N_2 -filled glovebox. Lattice parameters were refined by least-squares fitting using the CELL
279 software package⁵¹.

280

281 **Scanning electron microscopy (SEM).** A Philips XL30 ESEM-FEG instrument was used for SEM and
282 energy dispersive X-ray spectroscopy (EDX) characterisation. Experiments were performed in high
283 vacuum mode with an applied accelerating voltage of 15 kV. Samples were loaded onto aluminium
284 stubs using adhesive carbon tabs and the transfer was performed under a stream of flowing N_2 gas.

285

286 **Atomic force microscopy (AFM).** AFM sample preparation consisted of dispersing the samples in n-
287 propyl acetate (NPA) in an Ar-filled glove box. Then, a droplet of the concentrated Li_3N solution was
288 placed onto a silicon wafer for measurement. AFM analyses were carried out using a Keysight 5500
289 instrument in tapping mode, to produce topographical information of the samples.

290

291 **Transmission electron microscopy (TEM).** TEM analyses were performed using different instruments
292 under varying operating conditions. Measurements performed at 80 kV were conducted using a JEOL
293 JEM-2200MCO FEGTE. Samples were loaded in an N_2 -filled glovebox onto a custom-made air-tight
294 holder to minimise air exposure during transfer. Analyses performed at 200 kV were made using
295 either a JEOL JEM-2000FX II TEM or an FEI Tecnai G^2 20 TEM. TEM samples were prepared by
296 depositing the Li_3N dry onto a 3-mm holey carbon film copper grid in an N_2 -filled glovebox. Each grid
297 was placed within a sealed container and transferred to the instrument under a stream of N_2 . In both
298 cases, a small condenser aperture was used to reduce beam damage (the result of which is evident
299 in Supplementary Figure 12) and evaporation due to the instability of nanoscale Li_3N under the
300 beam.

301

302 **^7Li nuclear magnetic resonance (NMR) spectroscopy.** Wideline ^7Li NMR spectra of Li_3N
303 nanomaterials were recorded from 133 – 453 K at a Larmor frequency of 116.6 MHz on a Varian
304 InfinityPlus Spectrometer equipped with a single-resonance broadband probe. Spectra were
305 obtained using an EXORCYCLED solid-echo sequence with $\pi/2$ pulses of 1.3 μs and an echo delay of
306 16.0 μs . Relaxation delays between 0.5 and 10 s were used depending on the temperature. Chemical
307 shifts are referenced externally to aqueous LiCl.

308

309 **Raman spectroscopy.** Raman spectra were collected using a Horiba-Yvon LabRam HR confocal
310 microscope at room temperature using a 532 nm laser with a 600 gr mm^{-1} grating and a Synapse CCD

311 detector. Samples were mounted in sealed glass capillaries in an N₂-filled glovebox to avoid air
312 exposure. A 10 times reduced incident laser power (15 mW) was used together with a 100 nm
313 aperture to avoid damaging the material under the beam during analysis.

314

315 **Hydrogen storage measurements.** Volumetric hydrogen uptake measurements were performed by
316 loading ca. 0.2 g sample into a Swagelock tube in an N₂-filled glovebox and sealed using parafilm.
317 The tube was connected to the differential pressure analysis (DPA) apparatus⁵⁶ and the parafilm was
318 seal-broken using a flow of helium gas. The sample was evacuated before exposure to hydrogen and
319 heated to the reaction temperature. H_{2(g)} and He_(g) were dried using a liquid nitrogen trap before
320 use. Hydrogen uptake was performed at 10 bar at 200 °C. After reaching equilibrium the sample was
321 desorbed at 200 °C before performing the next absorption cycle.

322

323 **Density functional theory (DFT) calculations.** Electronic properties of bulk and nano-sheets of α-Li₃N
324 were calculated at the gradient-corrected DFT level by applying the Perdew-Burke-Ernzerhof (PBE)⁵²
325 exchange-correlation functional as implemented in the SIESTA program package⁵³. Electronic states
326 were expanded by a double-ζ plus polarization basis set with norm-conserving Troullier-Martins
327 pseudopotentials⁵⁴ for the description of core levels and a plane-wave representation of the charge
328 density with a cut-off of 240 Ry. The reciprocal space was sampled by a Monkhorst-Pack grid⁵⁵ of
329 16×16×32 k points in the Brillouin zone (16×16×1 k points in the case of nanosheets). Models of
330 nanosheets are composed of an increasing number of unit cell replicas constructed in the direction
331 perpendicular to the nano-sheet plane and a 15 Å thick vacuum region. Geometries of all systems
332 were relaxed until a maximum gradient of 0.02 eV Å⁻¹ on forces was reached. In the calculations of
333 the total energies of type I and type II nanofibres, the model structures were built with an increasing
334 number of replicas of the unit cell in the non-periodic directions to achieve the convergence in terms
335 of energy per number of replicas (14 replicas were used for type I nanofibre and 8×8 for type II
336 nanofibre). An MP k-points sampling with 16 k-points in the periodic directions has been applied
337 (two directions for type I nanofibre and one direction for type II nanofibre).

338

339 **Data availability**

340 The authors declare that the data supporting the findings of this study are
341 available within the paper and its supplementary information files.

342

343 **References**

- 344 1. Boukamp, B. A. and Huggins, R. A. Fast ionic conductivity in lithium nitride. *Mater. Res. Bull.* **13**,
345 23-32 (1978).
- 346 2. Shodai, T., Okada, S. Tobishima, S. and Yamaki, J. Study of Li_{3-x}M_xN (M: Co, Ni or Cu) system for
347 use as anode material in lithium rechargeable cells. *Solid State Ionics*, **86-88**, 785-789 (1996).
- 348 3. Hu, Y. H. and Huo, Y. Fast and exothermic reaction of CO₂ and Li₃N into C-N-containing solid
349 materials. *J. Phys. Chem. A* **115**, 11678-11681 (2011).
- 350 4. Duan L. *et al.* Thermally decomposable lithium nitride as an electron injection material for
351 highly efficient and stable OLEDs. *J. Phys. Chem. C* **113**, 13386-13390 (2009).
- 352 5. Baldwin, F. P., Blanchard, E. J. and Koenig, P. E. Metal nitrides in organic reactions. I. Reactions
353 of lithium nitride with acid chlorides. Preparation of N,N-diacylamides. *J. Org. Chem.* **30**, 671-
354 673 (1965).

- 355 6. Chen, P., Xiong, Z., Luo, J., Lin, J. and Tan, K. L. Interaction of hydrogen with metal nitrides and
356 imides. *Nature* **420**, 302-304 (2002).
- 357 7. Adams, P. F., Hubberstey and P. Pulham, R. J. Review of the solubility of nonmetals in liquid
358 lithium. *J. Less-Common Met.* **42**, 1-11 (1975).
- 359 8. Kimura, H., Asano M. and Kubo, K. Vaporization of solid lithium nitride. *J. Nucl. Mater.* **91**, 200-
360 204 (1980).
- 361 9. Stach, E. A. *et al.* Watching GaN nanowires grow, *Nano Lett.* **3**, 867-869 (2003).
- 362 10. Rodriguez, N. M., Chambers, A. and Baker, R. T. K. Catalytic engineering of carbon
363 nanostructures. *Langmuir*, **11**, 3862-3866 (1995).
- 364 11. Che, G., Lakshmi, B. B., Martin, C. R. and Fisher, E. R. Chemical vapor deposition based synthesis
365 of carbon nanotubes and nanofibres using a template method. *Chem. Mater.* **10**, 260-267
366 (1998).
- 367 12. Fortuna, S. A. and Li, X. Metal-catalysed semiconductor nanowires: a review on the control of
368 growth directions, *Semicond. Sci. Technol.* **25**, 024005 (2010).
- 369 13. a) Kuykendall, T. R., Altoe, M. V. P., Ogletree, F., Aloni, S. Catalyst-directed crystallographic
370 orientation control of GaN nanowire growth, *Nano Lett.* **14**, 6767-6773 (2014). b) D.-M. Tang, C.
371 Liu and H.-M. Chen, Controlled synthesis of quasi-one-dimensional boron nitride
372 nanostructures, *J. Mater. Res.* **22** (10), 2809-2816 (2007).
- 373 14. Lugstein, A., Steinmair, M., Hyun, Y. J., Hauer, G., Pongratz, P., Bertagnolli, E., Pressure-Induced
374 Orientation Control of the Growth of Epitaxial Silicon Nanowires. *Nano Lett.*, **8**, 2310-2314
375 (2008).
- 376 15. Madras, P., Dailey, E., Drucker J., Kinetically induced kinking of vapor-liquid-solid grown
377 epitaxial Si nanowires. *Nano Lett.*, **9**, 3826-3830 (2009).
- 378 16. Liu H., Shi, L., Geng, X., Su, R., Cheng, G., Xie, S. Reactant-governing growth direction of indium
379 nitride nanowires, *Nanotechnology*, **21**, 245601 (2010).
- 380 17. Shen, Y., Lebedev, O.I., Turner, S., Van Tendeloo, G., Song, X., Yu, X., Wang, Q., Chen, H.,
381 Dayeh, S.A., Wu, T. Size-Induced Switching of Nanowire Growth Direction: a New Approach
382 Toward Kinked Nanostructures. *Adv. Funct. Mater.* **26**, 3687-3695 (2016)
- 383 18. Chandrasekhar, H. R., Bhattacharya, G., Migoni and R., Bilz, H. Infrared and Raman spectra and
384 lattice dynamics of the superionic conductor lithium nitride (Li₃N). *Phys. Rev. B* **17**, 884-893
385 (1978).
- 386 19. Chandrasekhar, H. R., Bhattacharya, G., Migoni, R. and Bilz H. Phonon spectra and lattice
387 dynamics of lithium nitride. *Solid State Comm.* **22**, 681-684 (1977).
- 388 20. Nemanich, R. J. and Solin, S. A. First- and second-order Raman scattering from finite-size crystals
389 of graphite. *Phys. Rev. B* **20**, 392-401 (1979).
- 390 21. Nemanich, R. J. and Solin, S. A., Martin, R. M. Light scattering study of boron nitride
391 microcrystals. *Phys. Rev. B* **23**, 6348-6356 (1981).
- 392 22. Arenal, R. *et al.*, Raman Spectroscopy of single-wall boron nitride nanotubes. *Nano Lett.* **6**,
393 1812-1816 (2006).
- 394 23. Nesheva, D. Raman scattering from semiconductor nanoparticles and superlattices. *J.*
395 *Optoelectron. Adv. M.* **7**, 185-192 (2005).
- 396 24. Kress, W., Grimm, H., Press, W. and Lefebvre, J. Lattice vibrations in lithium nitride, Li₃N. *Phys.*
397 *Rev. B* **22**, 4620-4625 (1980).
- 398 25. R. Tenne, Inorganic nanotubes and fullerene-like materials. *Chem. Eur. J.* **8**, 5296-5304 (2002).
- 399 26. Messer, R., Birli, H. and Differt, K. NMR Study of diffusion in Li₃N. *J. Phys. C Solid State* **14**, 2731-
400 2746 (1981).

- 401 27. Stoeva, Z., Gomez, R., Gregory, D. H., Hix, G. B. and Titman, J. J. Evolution of structure, transport
402 properties and magnetism in ternary lithium nitridometalates $\text{Li}_{3-x-y}\text{M}_x\text{N}$, $\text{M} = \text{Co}, \text{Ni}, \text{Cu}$. *Dalton*
403 *Trans.* 3093–3097 (2004).
- 404 28. Jiang, C., Li, H., Wang, C. Recent progress in solid-state electrolytes for alkali-ion batteries. *Sci*
405 *Bull.* **62**, 1473-1490 (2017).
- 406 29. Chan, C. K., Yang, T., J. and Weller, J. M. Nanostructured Garnet-type $\text{Li}_7\text{La}_3\text{Zr}_2\text{O}_{12}$: Synthesis,
407 Properties and Opportunities as Electrolytes for Li-ion Batteries, *Electrochim. Acta* **253**, 268-280
408 (2017).
- 409 30. Rabenau, A. Lithium nitride and related materials case study of the use of modern solid state
410 research techniques. *Solid State Ionics*, **6**, 277-293 (1982).
- 411 31. David, W. I. F. *et al.* A Mechanism for Non-stoichiometry in the Lithium Amide/Lithium Imide
412 Hydrogen Storage Reaction. *J. Am. Chem. Soc.*, **129**, 1594-1601 (2007).
- 413 32. Demir-Cakan, R., Tang, W. S., Darwiche and Janot, A. R. Modification of the hydrogen storage
414 properties of Li_3N by confinement into mesoporous carbons. *Energy Environ. Sci.* **4**, 3625-3631
415 (2011).
- 416 33. Jiang, Z. P., Zhou, X., Sun, Q., Wang, Q. and Jena, P. Geometry, Electronic Properties, and
417 Hydrogen Adsorption Properties of Li_3N -Based Nanostructures, *J Phys. Chem. C* **14**, 19202–
418 19205 (2010).
- 419 34. Jin, H. M., Luo, J. Z. and Wu, P. Adsorption and dissociation of hydrogen on Li_3N surface: A first
420 principles study, *Appl. Phys. Lett.* **90**, 084101-1-084101-3 (2007).
- 421 35. Wu, S., Neo, S. S., Dong, Z., Boey, F. and Wu, P. Tunable ionic and electronic conduction of
422 lithium nitride via phosphorus and arsenic substitution: a first-principles study. *J. Phys. Chem. C*
423 **114**, 16706-16709 (2010).
- 424 36. Zhao, Y., Tian, X., Xue, W. and Gao, T. The structure, dynamical and thermodynamic properties
425 of $\alpha\text{-Li}_3\text{N}$: a first-principles study. *Solid State Comm.* **149**, 2130-2134 (2009).
- 426 37. Baumeier, B., Kruger, P., Pollmann, J. and Vajenine, G. V. Electronic structure of alkali-metal
427 fluorides, oxides, and nitrides: density-functional calculations including self-interaction
428 corrections. *Phys. Rev. B* **78**, 125111 (2008).
- 429 38. Dovesi, R., Pisani, C., Ricca, F., Roetti, C. and Saunders, V. R. Hartree-Fock study of crystalline
430 lithium nitride. *Phys. Rev. B* **30**, 972-979 (1984).
- 431 39. Brendecke, H. and Bludau, W. Photoluminescence properties of lithium nitride, *Phys. Rev. B* **21**,
432 805-815 (1980).
- 433 40. Sham, L. J. and Schlüter, M. Density-functional theory of the band gap. *Phys. Rev. B* **32**, 3883-
434 3889 (1985).
- 435 41. Sham, L. J. and Schlüter, M. Density-functional theory of the band gap. *Phys. Rev. Lett.* **51**, 1888-
436 1891 (1985).
- 437 42. Partoens, B. and Peeters, F. M. From graphene to graphite: electronic structure around the K
438 point. *Phys. Rev. B* **74**, 075404-1-075404-11 (2006).
- 439 43. Song, L. *et al.* Large Scale Growth and Characterization of Atomic Hexagonal Boron Nitride
440 Layers. *Nano Lett.*, **10**, 3209–3215 (2010).
- 441 44. Blase, X. *et al.* Quasiparticle band structure of bulk hexagonal boron nitride and related
442 systems. *Phys. Rev. B*, **51** 6868-6875 (1995).
- 443 45. Hoffman, D. M., Doll, G. L. and Eklund P. C. Optical properties of pyrolytic boron nitride in the
444 energy range 0.05—10 eV. *Phys Rev B*, **30**, 6051-6056 (1984).

- 445 46. Sun, Y., Li, Y., Sun, J., Li, Y., Pei, A. and Cui, Y. Stabilised Li₃N for efficient battery cathode
446 prelithiation. *Energy Storage Mater.* **6**, 119-124 (2017).
- 447 47. Bian, Z. Pang, Q., Wei, Y., Zhang, D., Gao, Y. and Chen, G. Dual roles of Li₃N as an Electrode
448 Additive for Li-Excess Layered Cathode Materials: A Li-Ion Sacrificial Salt and Electrode-
449 Stabilizing Agent. *Chem. Eur. J.* **24**, 13815-13820 (2018).
- 450 48. Park, K. and Goodenough, J. B. Dendrite-Suppressed Lithium Plating from a Liquid Electrolyte via
451 Wetting of Li₃N. *Adv. Energy Mater.* **7**, 1700732 (2017).
- 452 49. Baloch, M., Shanmukaraj, D., Bondarchuk, O., Bekaert, E., Rojo, T. and Armand, M. *Energy*
453 *Storage Mater.* **9** 141–149 (2017).
- 454 50. Barker, M. G., Begley, M. J., Edwards, P. P., Gregory, D. H. and Smith, S. E. Synthesis and crystal
455 structures of the new ternary nitrides Sr₃CrN₃ and Ba₃CrN₃. *J. Chem. Soc. Dalton Trans.* **1**, 1-5
456 (1996).
- 457 51. Holland, T. J. B. and Redfern, S. A. T. Unit cell refinement from powder diffraction data: the use
458 of regression diagnostics. *Mineral. Mag.* **61**, 65-77 (1997).
- 459 52. Perdew, J., Burke, K. and Ernzerhof, M. Generalized Gradient Approximation Made Simple.,
460 *Phys. Rev. Lett.* **77**, 3865–3868 (1996).
- 461 53. Soler, J. M. *et al.*, The SIESTA method for ab initio order-N materials simulation., *J. Phys.*
462 *Condens. Matter* **14**, 2745 (2002).
- 463 54. Troullier, N. and Martins, J. L. Efficient pseudopotentials for plane-wave calculations., *Phys. Rev.*
464 *B* **43**, 1993 (1991).
- 465 55. Monkhorst, H. J. and Pack, J. D. Special points for Brillouin-zone integrations., *Phys. Rev. B* **13**,
466 5188–5192 (1976).
- 467 56. Blackman, J. M., Patrick, J. W. and Snape, C. P. An accurate volumetric differential pressure
468 method for the determination of hydrogen storage capacity at high pressures in carbon
469 materials. *Carbon* **44**, 918-927 (2006).

470

471 **Acknowledgements**

472 DHG acknowledges the EPSRC for financial support under grants *GR/S26965* and *EP/E040071*, the
473 University of Nottingham for studentships for AGG and HKE, the University of Glasgow for a
474 studentship for CWD and ScotCHEM for a studentship for NTR. EB acknowledges a New Directions
475 for EPSRC Research Leaders Award (EP/G005060), the European Research Council under the
476 European Union's Seventh Framework Programme (FP7)/ERC grant agreement No. 307755-FIN and a
477 Royal Society Wolfson Fellowship for financial support. MB and EB acknowledge the use of Athena at
478 HPC Midlands+, which was funded by the EPSRC on grant EP/ P020232/1 as part of the HPC
479 Midlands+ consortium.

480

481 **Author contributions**

482 NTR, AGG, CMJ and CWD developed the synthesis methods and characterised materials by X-ray
483 diffraction, spectroscopy and electron microscopy; HKE, PDB and IM performed transmission
484 electron microscopy and electron diffraction experiments and analysed and interpreted these data;
485 JMB, CPS, CMJ and NTR performed hydrogen uptake experiments, analysed and interpreted these
486 data; MB and EB performed computational calculations, analysed, interpreted the data and
487 prepared these for publication; JJT designed the solid-state NMR experiments and collected and
488 interpreted the NMR data; DHG initiated and supervised the project and analysed and interpreted
489 the data. NTR, JJT, EB and DHG wrote the manuscript. All authors discussed the results and

490 commented on the paper.

491

492 **Competing Interests**

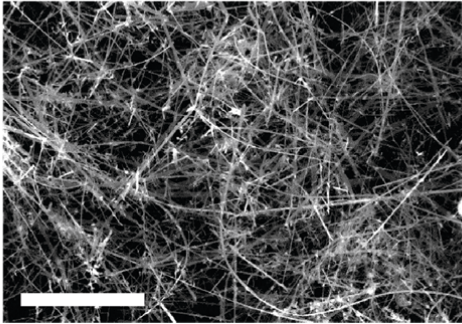
493 The authors declare no competing interests

494

495

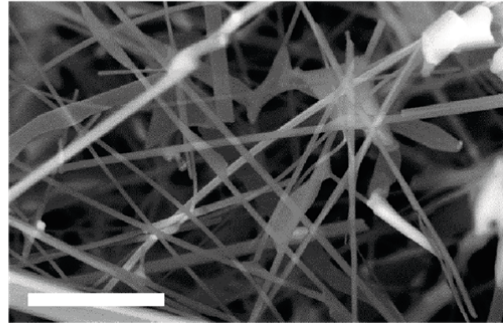
496 **Figures**

a



497

b

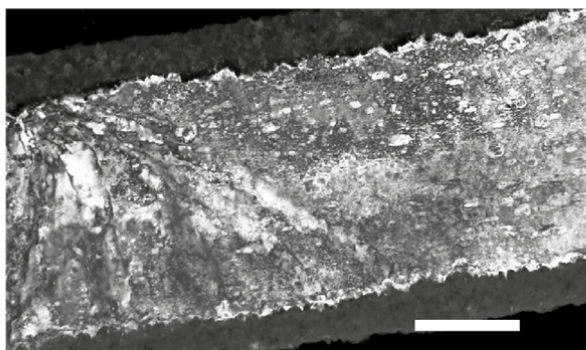
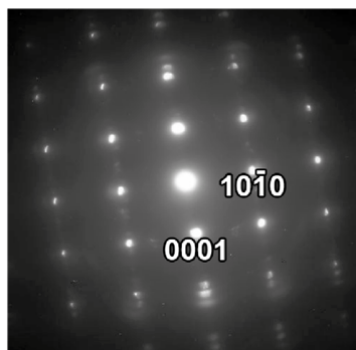
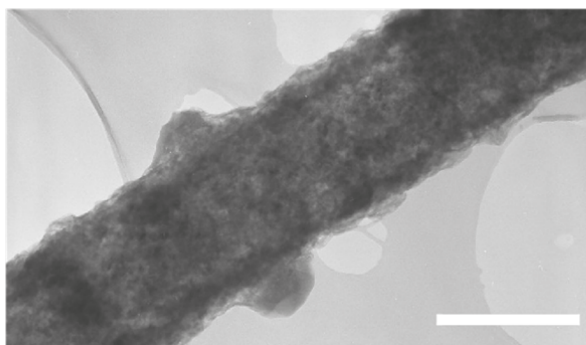
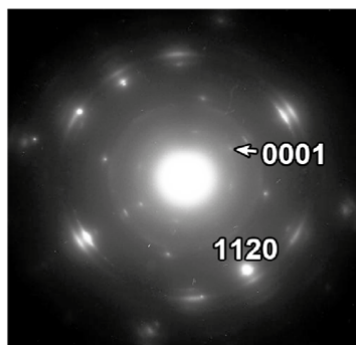


498 Figure 1. SEM micrographs of typical Li_3N nanofibres (type I) at different magnifications. Images are
499 taken at: a) x 500 and b) x 5000. Scale bars correspond to 50 μm (a) and 5 μm (b).

500

501

502

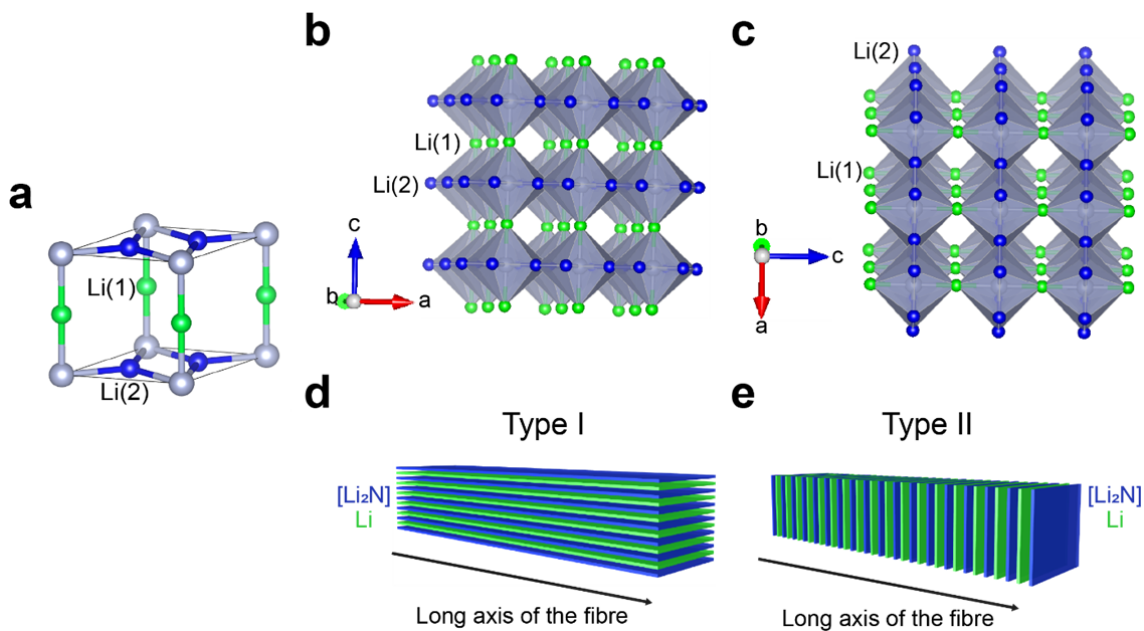
a**b****c****d**

503
504

505 Figure 2. Transmission electron microscopy (TEM) images and selected area electron diffraction
 506 (SAED) patterns of Type I and Type II fibres. a) High magnification bright field TEM image of a type I
 507 fibre (Li_3N core and an LiOH outer layer) and b) corresponding SAED pattern in the $\langle 2\bar{1}0 \rangle$ projection
 508 demonstrating the $\langle 10\bar{1}0 \rangle$ nanofibre growth direction; c) Bright field TEM image of a type II fibre
 509 and d) corresponding SAED pattern in the $\langle 01\bar{1}0 \rangle$ projection (with arcs due to an LiOH surface
 510 layer) showing the $\langle 0001 \rangle$ growth direction. Scale bars in a) and c) correspond to 500 nm.

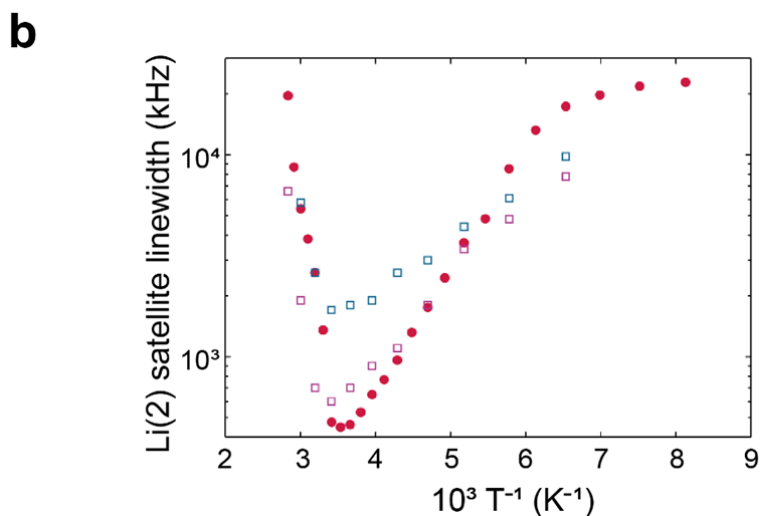
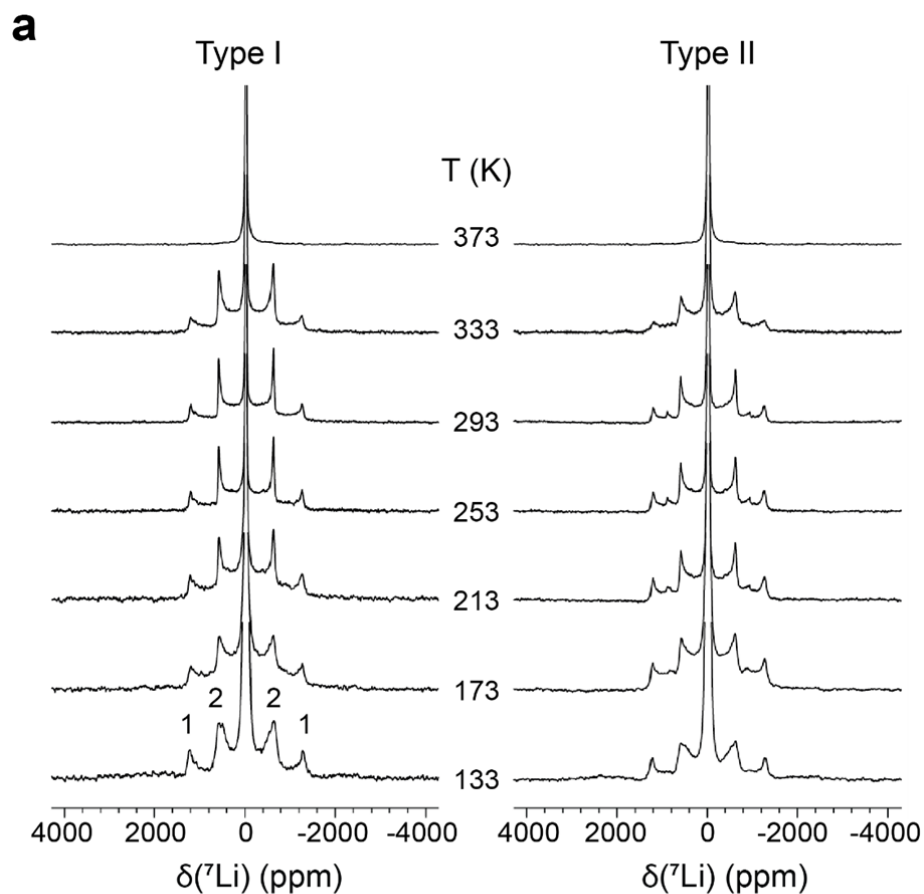
511

512



513

514 Figure 3. Schematic diagrams illustrating the Li_3N crystal structure and type I and type II nanofibres.
 515 a) Li_3N unit cell, showing Li(1) atoms (green spheres), Li(2) atoms (blue spheres) and N (grey
 516 spheres); Polyhedral representations of Li_3N showing Li(1) atoms and Li(2) atoms: b) aligned in the
 517 ab direction and c) perpendicular to the ab direction; Corresponding depictions of d) type I and e)
 518 type II Li_3N nanofibres, based on the orientation of the Li (green) and $[\text{Li}_2\text{N}]$ layers (blue) with respect
 519 to the long axis of the fibre.



520

521

522 Figure 4. ^7Li NMR characterisation at variable temperatures of type I and II fibres. a) Variable-

523 temperature (VT) ^7Li NMR spectra recorded between 133 K and 373 K for type I (left) and

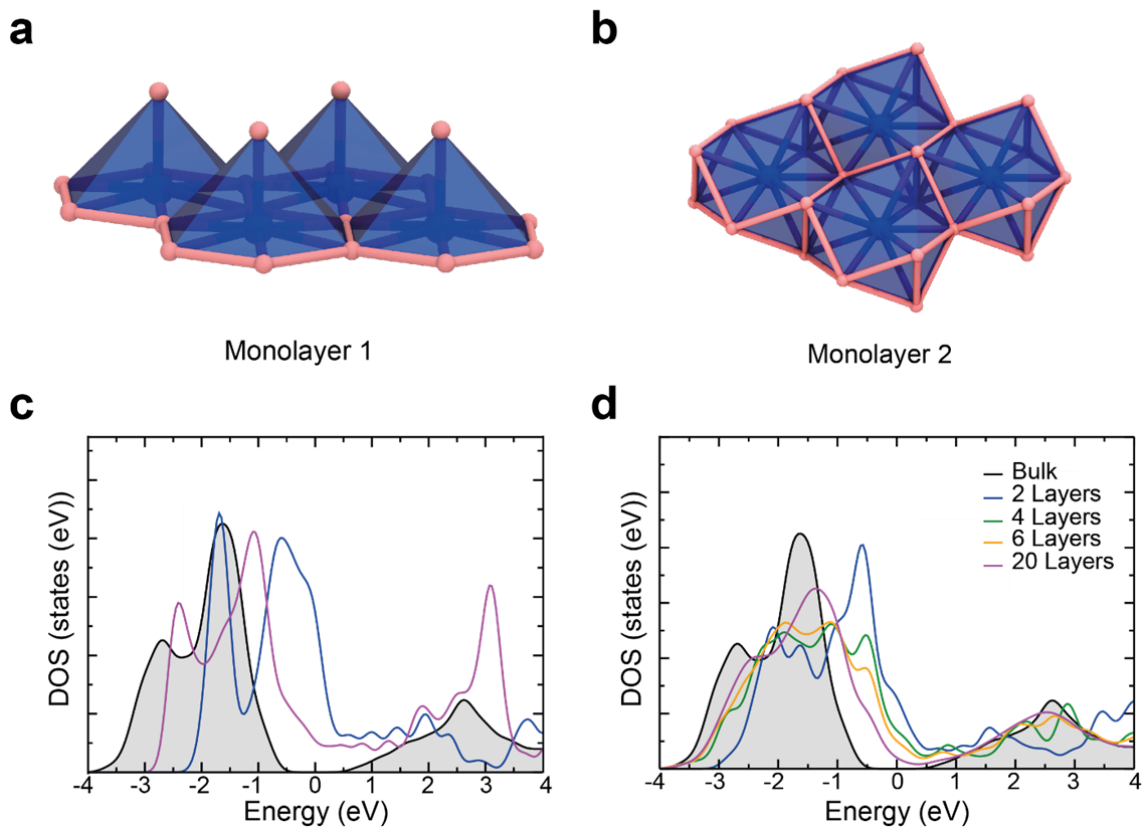
524 type II (right) Li_3N nanofibres. 1 and 2 denote satellite bands for the two-coordinate Li(1) site and

525 three-coordinate Li(2) site respectively; b) Temperature variation of the linewidth of the Li(2)

526 satellites for type I (magenta) and II (blue) Li_3N nanofibres and bulk Li_3N (red)⁴⁰ extracted from the

527 VT NMR by fitting a simulated powder lineshape.

528



529

530 Figure 5. Li_3N monolayer configurations and electronic structures determined from density
 531 functional theory calculations. Calculated Li_3N monolayer structures of: a) form 1; b) form 2; c)
 532 Comparison of the total DOS for bulk Li_3N (black) with form 1 (blue) and 2 (magenta) monolayers
 533 respectively; d) Evolution of the total DOS for increasing numbers of Li_3N layers (2 (blue); 4 (green); 6
 534 (yellow); and 20 (magenta)) as compared to that of the bulk material (black).